Stability of ion-beam-induced bixbyite phase in δ-Sc4Hf3O12 under heat treatments and electron beam irradiations

Manasari Iwasaki, Maulik Patel, Gianguido Baldinozzi, Kurt E. Sickafus, Manabu Ishimaru

Stability of ion-beam-induced bixbyite phase in δ-$Sc_4Hf_3O_{12}$ under heat treatments and electron beam irradiations

Masanari Iwasaki,[1] Maulik K. Patel,[2] Gianguido Baldinozzi,[3] Kurt E. Sickafus,[4] and Manabu Ishimaru[1,*]

[1]*Department of Materials Science and Engineering, Kyushu Institute of Technology, Fukuoka 804-8550, Japan*

[2]*Department of Mechanical, Materials, and Aerospace Engineering, The University of Liverpool, Liverpool L69 3GH, United Kingdom*

[3]*Structures, Propriétés et Modélisation des Solides, Université Paris-Saclay, CentraleSupelec, CNRS, 91190 Gif-sur-Yvette, France*

[4]*Materials Science and Technology Division, Los Alamos National Laboratory, Los Alamos, NM 87545, USA*

Abstract

Oxygen-deficient compounds $A_4B_3O_{12}$ have a δ-type structure with a regular long-range arrangement of oxygen vacancies induced by compensation of the charge difference between A^{3+} and B^{4+} cations, while A and B cations do not order long-range and only display weak short-range correlations. The δ-type compounds in the Sc_2O_3-HfO_2 and Sc_2O_3-ZrO_2 systems exhibit excellent resistance to radiation-induced amorphization, but the long-range ordered δ-phase was transformed into a short-range ordered bixbyite phase. Since this structural change was not predicted from the phase diagram, the validity of the formation of the bixbyite phase and its stability are still unclear. In the present study, the changes of radiation-induced microstructures in δ-$Sc_4Hf_3O_{12}$ under heat treatments and electron beam irradiations were examined by *ex-situ* and *in-situ* transmission electron microscopy. It was found that the ion-beam-induced metastable bixbyite phase is transformed into the δ and fluorite phases by the rearrangement of the oxygen vacancies.

*Corresponding author: ishimaru@post.matsc.kyutech.ac.jp

1. Introduction

Knowledge of structural changes under radiation environments is of technological importance for developing radiation tolerant materials for use in the nuclear industrial [1-7]. The radiation behavior of oxygen-deficient fluorite structural derivatives [8], such as pyrochlore ($M^{+3}_2M^{+4}_2O_7$, where M represents the metal species, and O is oxygen) [9-12], murataite [13,14], and *C*-type rare earth sesquioxide (bixbyite) (M_2O_3) [15-17], are extensively studied by many researchers, because oxide ceramics with a fluorite-type structure, such as uranium dioxide and zirconium dioxide often display exceptional radiation resistance. Pyrochlores that are ordered long-range have perfect arrangements of the cations and oxygen vacancies: therefore, they are an interesting playground to explore the effects of radiation on the long-range order of both sublattices. *A*, *B*, and *C*-type sesquioxides of rare earths are systems where there is no compositional cation disorder and only the vacancies in the anion sublattice can be disordered: they are therefore interesting to understand how radiation effects affect specifically this sublattice. Oxygen-deficient compounds $A_4B_3O_{12}$ possess a delta (δ) type structure with a regular long-range arrangement of oxygen vacancies, whereas A and B cations do not order long-range and only display weak short-range correlations. The tendency to develop short or long-range order in aliovalent doped fluorite systems can be related to the mean size and the size mismatch of the cations M. Size is parameterized by the cation radius r_M, and size mismatch is described by the statistical variance in the distribution of the radii, that is defined by $\sigma^2 = \langle r_M^2 \rangle - \langle r_M \rangle^2$, where the bracket represents the ensemble average. When two cations A and B share the same fluorite sublattice, such as $M = (A_{1-x}B_x)$, the expression of the variance reduces to $\sigma^2 = x(1-x)(r_A-r_B)^2$. In the case of $Sc_4Zr_3O_{12}$ and $Sc_4Hf_3O_{12}$, the variance σ^2 is only 1.5×10^{-4} and 3×10^{-4} respectively, much less than in systems that exhibit short-range or long-range cation order like for instance the defect fluorite $Ho_2Zr_2O_7$ ($\sigma^2=81\times10^{-4}$) and the ordered pyrochlore $Ho_2Ti_2O_7$ ($\sigma^2=225\times10^{-4}$). Therefore, these δ-type compounds are the ideal playground to understand the radiation effects on the anion sublattice in systems where the cation sublattice can be kept almost perfectly disordered.

The δ-type compounds exhibit an excellent radiation-induced amorphization resistance [18-20], and the pristine long-range ordered rhombohedral δ-phase transforms to a long-range disordered cubic oxygen-deficient fluorite phase. In this structure, cations and anion vacancies are statistically distributed onto the site

of their respective sublattices, a behavior consistent with the high temperature pseudo-binary phase diagram Sc_2O_3-ZrO_2 [18,21,22]. Interestingly, the formation of a short-range ordered cubic bixbyite phase is confirmed in 300 keV Kr^{2+} ion irradiated δ-$Sc_4Zr_3O_{12}$ [20] and 92 MeV Xe^{26+} ion irradiated δ- $Sc_4Hf_3O_{12}$ [23], indicating a non-binary response effect of the anion sublattice in this structure. The onset of the bixbyite order is unusual, because most of the radiation-induced structural changes involve a transformation from the low-temperature polymorph to a higher-temperature and higher symmetry one that is already present in the equilibrium phase diagram. However, several studies have not confirmed this phase transformation in irradiation experiments on δ phases: 185 MeV Au^{13+} ion irradiated $Sc_4Zr_3O_{12}$ to fluences ranging from 1×10^{11} to 1×10^{13} ions/cm^2 at room temperature [24]; 300 keV Kr^{2+} ion irradiated $Sc_4Zr_3O_{12}$ to fluence ranging from 1×10^{15} to 3×10^{16} ions/cm^2 at cryogenic temperature [19]; $Sc_4Hf_3O_{12}$ irradiated with 400 keV Ne^{2+} ions to fluences ranging from 1×10^{14} to 1×10^{15} ions/cm^2, 600 keV Kr^{3+} ions to fluences ranging from 5×10^{14} to 5×10^{15} ions/cm^2, and 6 MeV Xe^{26+} ions to fluences ranging from 2×10^{13} to 1×10^{15} ions/cm^2 [25]; 6 MeV Xe^{26+} ion irradiated $Lu_4Hf_3O_{12}$ to fluences ranging from 2×10^{13} to 1×10^{15} ions/cm^2 [26]. This means the formation mechanisms and the stability of the bixbyite phase remain open questions.

In irradiated δ-phases, the correlation length of the bixbyite phase is less than 10 nm, a value that largely exceeds the typical geometrical radius of the ion tracks obtained by transmission electron microscopy (TEM) experiments [23]. These domains with bixbyite order are embedded in a fluorite paracrystal with broken translational symmetry [20,23], so their presence can be visualized by TEM. TEM specimens are prepared by ion milling and focused ion beams, and the observed structures may also be sensitive to these processes. Also, the effects of temperature rise and electron beam irradiation can interfere with the TEM observations. In the present study, we examine specifically the behavior of the metastable bixbyite order under heat treatments and electron beam irradiation in ion-irradiated $Sc_4Hf_3O_{12}$.

2. Experimental

Polycrystalline $Sc_4Hf_3O_{12}$ pellets were prepared by sintering and confirmed to have the δ-type structure by x-ray diffraction. Details of the sample synthesis are described elsewhere [23,27]. The sintered pellets were

irradiated with 92 MeV Xe^{26+} ions to a fluence of 1×10^{14} cm^{-2} at room temperature using IRRSUD beamline at GANIL (Grand Accélérateur National d'Ions Lourds) in Caen, France. The ion flux was kept at 1×10^{9} ions/cm^{-2} s^{-1} while the sample surface was kept normal to the ion beam direction. The energy loss due to electronic and nuclear (displacive) interactions is estimated to be ~20 and ~1 keV/nm, while the projected range of 92 MeV Xe is estimated to be ~8 μm. The complete SRIM profiles and calculated integrated energy loss from these components is reported in Ref. 27. Some of the irradiated δ-$Sc_4Hf_3O_{12}$ pellets were annealed at 300 ºC for 2 hr under ambient atmosphere. The irradiated and annealed pellets were fabricated into cross-sectional TEM specimens. They were thinned to less than 10 μm by mechanical polishing in the cross-sectional direction using a tripod polisher, and then subjected to argon ion milling. To investigate the effects of induced heating during TEM sample preparation on microstructures, ion milling was performed at room and cryogenic temperatures. The TEM samples were carbon coated to avoid charge-up during observations. The cross-sectional TEM specimens were characterized by TEM using JEOL JEM-3000F and JEM-F200. To examine the stability of ion irradiation induced microstructures under electron beam environments, the latter instrument was operated at acceleration voltages of 200 and 80 kV. A heating holder was used for *in-situ* TEM observations of thermally-induced structural changes.

3. Results and discussion

A. Effects of ion milling on microstructures induced by ion irradiation

Figure 1 shows cross-sectional bright-field (BF) TEM images of ion irradiated δ-$Sc_4Hf_3O_{12}$. A 92 MeV Xe-ion beam was impinging from the left side, and the sample surface is located at a depth of 0 nm. The TEM specimens were prepared by ion milling at (a) room temperature and (b) cryogenic temperature. The former result has been already reported [23], but it is shown here for ease of comparison. In addition to the diffraction contrast due to crystal grains, a contrast change indicated by a white line is observed in both specimens. Note that, while the projected range is ~8 μm all TEM results presented, in the manuscript are shown only up to 6 μm to emphasis the role of electronic stopping. An interface contrast was observed at a depth of (a) ~4.5 and (b) ~5.0 μm from the surface where the electronic stopping power is ~22 and ~16 times larger than the nuclear

stopping power, respectively [23]. Thus, the irradiated region shows two distinct areas of interest separated by the contrast line, beyond which is the pristine region (not shown) of the samples.

We have previously reported that the crystal structures change crossing this line where the contrast is modified [23]. Figures 1(c) and 1(d) show selected-area electron diffraction (SAED) patterns taken from just above the contrast interface of Figs. 1(a) and 1(b), respectively. (See previous reports for electron diffraction patterns of the fluorite, bixbyite, and δ-type structures [20,23].) Superlattice reflections due to the ordering of oxygen vacancies are present in both diffraction patterns, and they can be indexed by a bixbyite-type structure (zone axis [011] and [111], respectively). On the other hand, the structure just below the contrast interface is different in the specimens prepared at room and at cryogenic temperature ion milling. Only the fundamental lattice reflections indexed by a fluorite lattice are observed in Fig. 1(e), whereas there are superlattice reflections indexed by a δ-type structure in Fig. 1(f). Since the projected range of the impinging ions is about 8 μm, the structures of Figs. 1(e) and 1(f) correspond to the region above the Bragg peak of the Xe ions, where the nuclear stopping contribution to the overall damage starts to increase, but where Xe implantation is still modest.

To investigate the microstructural changes at the interface in more detail, dark-field (DF) TEM observations were performed. The DF images of the specimen prepared by ion milling at room temperature can be found in Ref. 23, so only the results of cryogenic ion milling are shown here. In Fig. 2, the sample surface is still on the left side of the picture. The DF image taken with the fundamental lattice reflection shows an overall bright contrast (Fig. 2(a)), demonstrating that all the atoms of this region can scatter coherently. Figures 2(b) and 2(c) show the DF images taken with the superlattice reflection due to the δ and bixbyite structures, respectively. The side below the interface (right side of the image) presents a uniform bright contrast in Fig. 2(b), while only dispersed bright dots are observed above the contrast interface (left side of Fig. 2(c)). This is consistent with the short correlation length characteristic of this bixbyite phase: the bright domains of this image correspond to one set of the 16 possible variants of the bixbyite subgroup $Ia\bar{3}$ of $Fm\bar{3}m$. A high-resolution TEM image taken from the surface of the irradiated specimen is shown in Fig. 3. On closer examination, dark dots are regularly arranged in region A. The fast Fourier transform (FFT) diagram of this

region A is consistent with the (111) diffraction pattern of a single domain orientation of the bixbyite structure. On the other hand, the FFT diagram of the other regions of the pictures as for instance the one labeled B produce a diffraction pattern typical of a fluorite phase, demonstrating that these regions do not correspond to single domains of bixbyite structure but to at least two translational variants of bixbyite structure scattering coherently and with a same average fluorite zone axis. This indicates that the bixbyite domains are described by the cosets of $I\mathrm{a}\bar{3}$ in $F\mathrm{m}\bar{3}\mathrm{m}$. A similar bixbyite domain structure was also observed in δ-$Sc_4Hf_3O_{12}$ irradiated with 300-keV krypton ions where binary collisions dominate the physics of radiation damage [20].

B. *Ex-situ* and *in-situ* TEM observations of thermally-induced structural changes

As mentioned above, the bixbyite phase order was observed beneath the surface in both the specimens prepared by ion milling at room and at cryogenic temperatures, in the region where the radiation damage has an almost exclusive electronic origin. On the other hand, different structures occur in the region just below the contrast interface in samples prepared using the two different ion milling conditions. This suggests that the metastable stacking of oxygen vacancies in the bixbyite phase can reorganize following the temperature rise during ion milling. To confirm the validity of this speculation, thermally-annealed specimens were investigated. Figure 4 shows SAED patterns of the ion-irradiated δ-$Sc_4Hf_3O_{12}$ after heat treatment at 300 ^{o}C. Two types of diffraction patterns were obtained in a specimen prepared by ion milling at liquid nitrogen temperature and then submitted to thermal annealing, as shown in Figs. 4(a) and 4(b). They correspond to the $(\bar{1}11)$ and (112) reciprocal lattice planes of the δ-type and average fluorite structures, respectively. The positions of the fundamental average fluorite reflections are common to the two patterns, suggesting that the cations of the two regions can scatter coherently, and showing that the two patterns only involve a different arrangement of the oxygen vacancies. Interestingly, no diffraction pattern corresponding to the order of vacancies characteristic of the metastable bixbyite structure was observed after thermal annealing. This suggests that the metastable bixbyite order is lost after annealing, resulting in a phase where the oxygen vacancies are now either randomly distributed, or they adopt the stacking rules of the pristine rhombohedral δ-structure. Figure 4(c) shows a BF image of the specimen annealed at 300 ^{o}C, where the oxygen vacancy correlations of bixbyite type were

originally present in the as-irradiated state. In addition to a mottled contrast, a grain boundary indicated by arrows is observed in the specimen. Figure 4(d) shows a DF image taken using the superlattice reflection of the δ-phase, which is the identical area of Fig. 4(c). The bright and dark regions correspond to the δ and fluorite regions of spatial correlations for the oxygen vacancies, respectively. It was found that δ phase correlations are preferentially restored near the grain boundary.

Figure 5 shows the time evolution of SAED patterns under heat treatments obtained by *in-situ* TEM observations. Diffuse spots due to short-range ordered bixbyite are observed before thermal annealing in the (103) diffraction patterns of Fig. 5(a). The structures were maintained at 180 ^{o}C for 5 min (Fig. 5(b)), whereas sharp strong spots appear after annealing at 200 ^{o}C for 5 min (Fig. 5(c)). The intensity of the superlattice spots increases as annealing proceeds (Fig. 5(d)). These superlattice spots can be interpreted by the superposition of $(1\bar{1}2)$ reciprocal lattice planes of the δ-type structure with different variants. Finally, the diffuse spots of the bixbyite phase completely disappear after 15-min annealing (Fig. 5(e)). The *in-situ* observations were conducted in vacuum inside TEM, while the heat treatment of Fig. 4 was performed at atmospheric pressure. Regardless of the atmosphere, it was found that the bixbyite phase transforms to the disordered fluorite and/or ordered δ phases. This suggests that the structural changes observed here is not due to compositional effects but to rearrangements of oxygen vacancies. Indeed, no compositional difference was detected between the bixbyite, fluorite, and δ phases by energy-dispersive x-ray spectroscopy [23,28].

C. Stability of the bixbyite phase under electron beam irradiation

Figure 6 shows the change of the SAED pattern under 200-keV electron beam irradiation at room temperature. In addition to the fundamental fluorite lattice reflections, diffuse spots due to the bixbyite structure were observed in the area affected by ion irradiation (Fig. 6(a)). As the electron beam irradiation progresses (Fig. 6(b), then Fig. 6(c), and Fig. 6(d)), new sharper spots appear while the diffuse bixbyite spots become increasingly weaker. The new superlattice reflections, arranged in a ring around the main average fluorite lattice spots, correspond to different ferroelastic variants of the δ phase structure. To explain the SAED pattern of Fig. 7(a), nanobeam electron diffraction experiments were performed. Figures 7(b) and 7(c) show nanobeam

electron diffraction patterns obtained with an electron beam of ~50 nm diameter, taken from different regions of the electron-beam-irradiated area. These patterns correspond to (001) reciprocal lattice planes of the δ-type structure, but their orientations are different. Indeed, the corresponding DF images in Figs. 7(b') and 7(c'), formed by selecting superlattice spot in Figs. 7(b) and 7(c), respectively, clearly show the presence of two δ phase variants. Figure 7(a') shows the DF image obtained using two superlattice spots belonging to different variants. The dashed line indicates a part of the circle corresponding to the electron beam cross section. Although two different spots are used for the imaging, dark regions exist in the irradiated area. This suggests that in parts of the sample the bixbyite correlations among vacancies are indeed lost after annealing, but that the δ phase correlations of the pristine phase are not restored. In these regions, the oxygen vacancies remain disordered, leading to an oxygen deficient average fluorite structure.

Figure 8 shows a series of snapshots of *in-situ* DF TEM images captured from the video (see supplementary material, Fig. S1). To suppress thin-foil effects, thicker regions of the sample were observed with an electron beam at an acceleration voltage of 300 kV. In addition, the samples were irradiated at low doses to delay structural changes. An objective aperture was inserted into a superlattice spot due to the δ phase. Only the bixbyite and fluorite phases are present before electron beam irradiation, so the overall contrast in Fig. 8(a) is very weak. After irradiation, bright contrast regions appear in some places in Fig. 8(b), suggesting nucleation of the δ phase. The number of nucleation increases and the growth of the δ phase progresses with irradiation, as seen in Figs. 8(c-f). The bright contrast becomes stronger with irradiation, suggesting that the degree of order, i.e. the ordering of oxygen vacancies, becomes more pronounced.

The structural changes under electron beam irradiation are induced by two effects [29]: knock-on and electron excitation effects. The former is suppressed with decreasing the acceleration voltage of TEM, while the latter becomes more pronounced. To identify the mechanism of the electron-beam-induced structural changes, we examine the effects of the acceleration voltage of TEM on the stability of the bixbyite. The maximum recoil energy T_m is given by

$$T_m = 2E(E+2m_0c^2)/Mc^2,$$

where E is the energy of the incident electron, m_0 the rest mass of the electron, c the velocity of light, and M

the mass of the displaced atom. No report is available about knock-on energies of the constitute elements of δ-$Sc_4Hf_3O_{12}$, but typical threshold displacement energies for ceramics are in the range of 20-60 eV [30]. A 200-keV electron transfers energy up to 11.7 eV for a Sc atom, 2.9 eV for a Hf atom, and 32.8 eV for an O atom, suggesting that O atoms are far more likely to be displaced than other atoms in the irradiation conditions of Fig. 6. Assuming a threshold displacement energy of 20 eV, no knock-on effect occurs at acceleration voltages below 130 kV. Figure 9 shows SAED patterns (a) before and (b) after irradiation with 80-keV electron beams at the same flux as in Fig. 6. The diffuse spots due to the bixbyite structure are still observed after irradiation for 30 min and the formation of the δ-phase is significantly delayed. This suggests that the bixbyite-to-δ phase transformation under electron beam irradiation is due to knock-on effects rather than electron excitation one. Also, the 200-keV electron beam preferentially displaces anions, and has no significant effect over the cations. This consistently supports the conclusion that the observed structural changes are not cation rearrangements but only involve the rearrangement of the oxygen vacancies by knock-on effects.

As described above, the ion-beam-induced bixbyite phase is thermally metastable, and therefore we can also provide an estimate of the temperature rise during the electron beam irradiation. The heating effects under a uniformly distributed electron beam with a radius of r_0 can be estimated by the following equation [31]:

$$\Delta T = V_0 I_0 / \pi \kappa r_0,$$

where ΔT is the temperature rise, V_0 the acceleration voltage, I_0 the beam current, and κ the thermal conductivity. The values of κ are 3 $Wm^{-1}K^{-1}$ for ZrO_2 and 17 $Wm^{-1}K^{-1}$ for Sc_2O_3. The thermal conductivity for δ-$Sc_4Hf_3O_{12}$ is currently unknown, but it is probably greater than that of ZrO_2 due to the Sc_2O_3 richness: we used the value of κ for ZrO_2 to estimate the maximum temperature rise. Under the irradiation conditions of Fig. 6 (V_0 = 200 kV; I_0 = 1.5 nA; r_0 = 1.7 μm), the temperature rise was calculated to be ~20 K. This suggests that the observed structural changes induced by the electron beam are not thermal effects.

The structural changes observed here can be compared to other compounds containing atom-deficient sublattices. In nitrogen-deficient niobium nitride (NbN_{1-x}), several ordered structures appear depending on temperature and composition [32]. 300-keV electron beam irradiations cause a change from the

ordered tetragonal γ-phase to the disordered cubic δ-phase due to knock-on displacement of nitrogen atoms [33]. This structural change can be predicted based on the temperature-composition phase diagram: electron beam irradiation induces the transformation of the low-temperature phase into the high-temperature one.

In $YBaCuO_{7-y}$, the decrease of the superconducting critical temperature upon electron beam irradiation was attributed to the oxygen disordering [34]. A transformation from a low-symmetry phase to a high-symmetry phase due to vacancy disordering on the atom deficient sublattices was observed in electron irradiated vanadium oxides ($V_{1-x}O$) [35] and in vanadium carbides (VC_{1-x}) [36]. In the current system, the transformation from the bixbyite to δ-phase does not involve a group-subgroup relationship: therefore, the transformation is reconstructive and it involves the breakdown and reconstruction of the primary chemical bonds. The general theory of reconstructive phase transitions [37] predicts that these transitions are "sluggish" and in the present case it requires the existence of an intermediate disordered fluorite phase. This explains completely the actual observation of coexistence of the δ and the disordered fluorite phases. A more extensive study of the implications of this complex transformation pathway over the properties of this system is currently underway.

The picture of an emerging mesoscale organization obtained from these investigations suggests that there might be a need to scale up the future computational efforts over longer time and spatial scales. The emerging response of the anion sublattice of these systems seems highly correlated and non-local, suggesting a non-equilibrium time-dependent physics that is still significantly evolving after the initial radiation response of the system is largely completed. These emergent phenomena can be framed as dissipative structures arising from the far-from-equilibrium conditions [38].

4. Conclusions

Radiation-induced structures of δ-$Sc_4Hf_3O_{12}$ as well as their changes under heat treatments and electron beam irradiation were examined by *ex-situ* and *in-situ* TEM observations. Cross-sectional TEM observations revealed that short-range ordered bixbyite clusters are dispersed in the fluorite matrix from the surface to a depth of ~5 μm in the δ-$Sc_4Hf_3O_{12}$ irradiated with 92 MeV Xe ions a fluence of 1×10^{14} cm^{-2} at room

temperature. The ion-beam-induced bixbyite phase was highly susceptible for the temperature rise during ion milling, and was transformed into the δ and fluorite phases. Electron beam irradiation suggested that the structural change observed here was not cation rearrangements but only involve the rearrangement of the oxygen vacancies.

Acknowledgements

This work was supported in part by Grant-in-Aid for Scientific Research (B) (Grant No. 19H02463) from the Ministry of Education, Sports, Science, and Technology, Japan (MI). This work was also supported by JKA and its promotion funds from KEIRIN RACE (Grant No. 2023M-310) (MI). The TEM observations using JEOL JEM-F200 were performed at the Center for Instrumental Analysis, Kyushu Institute of Technology. We would like to thank Dr. Clara Grygiel of the GANIL and CIMAP for assistance and support in using beamline IRRSUD and Mr. Yusuke Kanazawa of Kyushu Institute of Technology for some of the TEM observations.

References

[1] G.R. Odette, M.J. Alinger, and B.D. Wirth, Recent developments in irradiation-resistant steels, Annu. Rev. Mater. Sci. 38 (2008) 471-503.

[2] S. J. Zinkle and J. T. Busby, Structural materials for fission & fusion energy, Mater. Today, 12 (2009) 12-19.

[3] K. L. Murty and I. Charit, Structural materials for Gen-IV nuclear reactors: Challenges and opportunities, J. Nucl. Mater. 383 (2008) 189-195.

[4] W. J. Weber, R. C. Ewing, C. R. A. Catlow, T. Diaz de la Rubia, L. W. Hobbs, C. Kinoshita, Hj. Matzke, A. T. Motta, M. Nastasi, E. K. H. Salje, E. R. Vance, and S. J. Zinkle, Radiation effects in crystalline ceramics for the immobilization of high-level nuclear waste and plutonium, J. Mater. Res. 13 (1998) 1434-1484.

[5] R. C. Ewing, W. J. Weber, and J. Lian, Nuclear waste disposal - pyrochlore ($A_2B_2O_7$): Nuclear waste form for the immobilization of plutonium and "minor" actinides, J. Appl. Phys. 95 (2004) 5949-5971.

[6] W. J. Weber, A. Navrotsky, S. Stefanovsky, E. R. Vance, and E. Vernaz, Materials science of high-level nuclear waste immobilization, MRS Bulletin 34 (2009) 46-53.

[7] K. E. Sickafus, L. Minervini, R. W. Grimes, J. A. Valdez, M. Ishimaru, F. Li, K. J. McClellan, and T. E. Hartmann, Radiation tolerance of complex oxides, Science 289 (2000) 748-751.

[8] K. E. Sickafus, R. W. Grimes, S. M. Corish, A. R. Cleave, M. Tang, C. R. Stanek, B. P. Uberuaga, and J. A. Valdez, Los Alamos Series Report #LA-14205: Layered Atom Arrangements in Complex Materials (Los Alamos National Laboratory, Los Alamos, NM, 2006).

[9] M. Lang, F. Zhang, J. Zhang, J. Wang, J. Lian, W J. Weber, B. Schuster, C. Trautmann, R. Neumann, and R. C. Ewing, Review of $A_2B_2O_7$ pyrochlore response to irradiation and pressure, Nucl. Instrum. Meth. Phys. Res. B 268 (2010) 2951-2959.

[10] J. Lian, X. T. Zu, K. V. G. Kutty, J. Chen, L. M. Wang, and R. C. Ewing, Ion-irradiation-induced amorphization of $La_2Zr_2O_7$ pyrochlore, Phys. Rev. B 66 (2002) 054108 (5 pages).

[11] N. J. Hess, B. D. Begg, S. D. Conradson, D. E. McCready, P. L. Gassman, and W. J. Weber, Spectroscopic

investigations of the structural phase transition in $Gd_2(Ti_{1-y}Zr_y)_2O_7$ pyrochlores, J. Phys. Chem. B 106 (2002) 4663-4677.

[12] C. Kinsler-Fedon, L. Nuckols, C. T. Nelson, Z. Qi, Q. Huang, D. Mandrus, Y. Zhang, W. J. Weber, and V. Keppens, Effects of Au^{2+} irradiation induced damage in a high-entropy pyrochlore oxide single crystal, Scr. Mater. 220 (2022) 114916 (5 pages).

[13] J. Lian, L. M. Wang, R. C. Ewing, S. V. Yudintsev, and S. V. Stefanovsky, Ion-beam-induced amorphization and order-disorder transition in the murataite structure, J. Appl. Phys. 97 (2005) 113536 (8 pages).

[14] A. A. Lizin, S. V. Tomilin, S. S. Poglyad, E. A. Pryzhevskaya, S. V. Yudintsev, and S. V. Stefanovsky, Murataite: a matrix for immobilizing waste generated in radiochemical reprocessing of spent nuclear fuel, J. Radioanal. Nucl. Chem. 318 (2018) 2363-2372.

[15] M. Tang, J. A. Valdez, P. Lu, G. E. Gosnell, C. J. Wetteland, and K. E. Sickafus, A cubic-to-monoclinic structural transformation in the sesquioxide Dy_2O_3 induced by ion irradiation, J. Nucl. Mater. 328 (2004) 71-76.

[16] C. L. Tracy, M. K. Lang, F. Zhang, C. Trautmann, and R. C. Ewing, Phase transformations in Ln_2O_3 materials irradiated with swift heavy ions, Phys. Rev. B 92 (2015) 174101 (14 pages).

[17] A. P. Solomon, C. L. Tracy, E. C. O'Quinn, D. Severin, and M. K. Lang, Transformations to amorphous and X-type phases in swift heavy ion-irradiated Ln_2O_3 and Mn_2O_3, J. Appl. Phys. 129 (2021) 225903 (10 pages).

[18] K. E. Sickafus, R. W. Grimes, J. A. Valdez, A. Cleave, M. Tang, M. Ishimaru, S. M. Corish, C. R. Stanek, and B. P. Uberuaga, Radiation-induced amorphization resistance and radiation tolerance in structurally related oxides, Nature Mater. 6 (2007) 217-223.

[19] J. A. Valdez, M. Tang, and K. E. Sickafus, Radiation damage effects in δ-$Sc_4Zr_3O_{12}$ irradiated with Kr^{2+} ions under cryogenic conditions, Nucl. Instrum. Meth. Phys. Res. B 250 (2006) 148-154.

[20] M. Ishimaru, Y. Hirotsu, M. Tang, J. A. Valdez, and K. E. Sickafus, Ion-beam-induced phase transformations in δ-$Sc_4Zr_3O_{12}$, J. Appl. Phys. 102 (2007) 063532 (7 pages).

[21] R. Ruh, H. J. Garrett, R. F. Domagala, and V. A. Patel, The system zirconia-scandia, J. Am. Ceram. Soc. 60 (1977) 399-403.

[22] H. M. Ondik and H. F. McMurdie, Phase Diagrams for Zirconium and Zirconia Systems (American Ceramic Society, Columbus, 1998).

[23] M. Iwasaki, Y. Kanazawa, D. Manago, M. K. Patel, G. Baldinozzi, K. E. Sickafus, and M. Ishimaru, Anomalous structural phase transformation in swift heavy ion-irradiated δ-$Sc_4Hf_3O_{12}$, J. Appl. Phys. 132 (2022) 075901 (8 pages).

[24] M. Tang, P. Kluth, J. Zhang, M. K. Patel, B. P. Uberuaga, C. J. Olson Reichhardt, and K. E. Sickafus, Swift heavy ion irradiation-induced microstructure modification of two delta-phase oxides: $Sc_4Zr_3O_{12}$ and $Lu_4Zr_3O_{12}$, Nucl. Instrum. Meth. Phys. Res. B 268 (2010) 3243-3247.

[25] J. Wen, Y. H. Li, M. Tang, J. A. Valdez, Y. Q. Wang, M. K. Patel, and K. E. Sickafus, Heavy and light ion irradiation damage effects in *δ*-phase $Sc_4Hf_3O_{12}$, Nucl. Instrum. Meth. Phys. Res. B 365 (2015) 325-330.

[26] J. Wen, C. Gao, Y. H. Li, Y. Q. Wang, L. M. Zhang, B. T. Hu, L. J. Chen, and X. Su, Ion irradiation induced order-to-disorder transformation in *δ*-phase $Lu_4Hf_3O_{12}$, Nucl. Instrum. Meth. Phys. Res. B 310 (2013) 1-5.

[27] M. K. Patel, K. E. Sickafus, and G. Baldinozzi, Divergent short- and long-range behavior in ion-irradiated *δ*-$Sc_4Hf_3O_{12}$, Phys. Rev. Mater. 4 (2020) 093605 (9 pages).

[28] K. E. Sickafus, M. Ishimaru, Y. Hirotsu, I. O. Usov, J. A. Valdez, P. Hosemann, A. L. Johnson, and T. T. Thao, Compositional analyses of ion-irradiation-induced phases in *δ*-$Sc_4Zr_3O_{12}$, Nucl. Instrum. Meth. Phys. Res. B 266 (2008) 2892-2897.

[29] N. Jiang, Electron beam damage in oxides: a review, Rep. Prog. Phys. 79 (2016) 016501 (33 pages).

[30] S. J. Zinkle and C. Kinoshita, Defect production in ceramics, J. Nucl. Mater. 251 (1997) 200-217.

[31] M. Liu, L. Xu, and X. Lin, Heating effect of electron beam bombardment, Scanning 16 (1994) 1-5.

[32] K.-Y. Liou and P. Wilkes, The radiation disorder model of phase stability, J. Nucl. Mater. 87 (1979) 317-330.

[33] J. H. Won, J. A. Valdez, M. Naito, M. Ishimaru, and K. E. Sickafus, Transmission electron microscopy study of an electron-beam-induced phase transformation of niobium nitride, Scr. Mater. 60 (2009) 799-802.

[34] S. K. Tolpygo, J.-Y. Lin, M. Gurvitch, S. Y. Hou, and J. M. Phillips, Effect of oxygen defects on transport properties and T_c of $YBa_2Cu_3O_{6+x}$: Displacement energy for plane and chain oxygen and implications for irradiation-induced resistivity and T_c suppression, Phys. Rev. B 53 (1996) 12462-12474.

[35] P. S. Bell and M. H. Lewis, Disordering of a vanadium monoxide superstructure by electron irradiation, Philos. Mag. 29 (1974) 1175-1187.

[36] J. D. Venables and R. G. Lye, Radiation damage of ordered V_6C_5 by electron microscope beam bombardment, Philos. Mag. 19 (1968) 565-582.

[37] P. Tolédano and V. Dmitriev, "Reconstructive Phase Transitions : In Crystals and Quasicrystals", World Scientific (1996).

[38] G. Nicolis and I. Prigogine, "Self-Organization in Nonequilibrium Systems: From Dissipative Structures to Order through Fluctuations", Wiley, New York (1977).

Figure captions

Figure 1. Cross-sectional TEM images of swift heavy ion irradiated δ-$Sc_4Hf_3O_{12}$ prepared by ion milling at (a) room temperature and (b) cryogenic temperature. A contrast interface is present at the position indicated by a line. Selected-area electron diffraction patterns taken from (c,d) just above and (e,f) below the interface. The diffraction patterns of (c) and (d) are in agreement with those of the bixbyite structure viewed along the [011] and [111] directions, respectively. The diffraction patterns of (e) and (f) correspond to those of the average fluorite and δ-type structures, respectively.

Figure 2. Dark-field TEM images near the interface of ion irradiated δ-$Sc_4Hf_3O_{12}$ prepared by ion milling at cryogenic temperature. The images were taken using (a) the fundamental lattice spot, (b) the superlattice spot of the δ-structure, and (c) the superlattice spot of the bixbyite structure. It is apparent that the regions of the δ and bixbyite/average fluorite phases are clearly separated. A cluster of δ phase in the bixbyite/ average fluorite ensemble average of several domains appears to be due to electron beam irradiation during beam alignment in (b).

Figure 3. A high-resolution TEM image taken from the surface of the irradiated region and FFT diagram obtained from the square area. In addition to bright dots, dark dots are observed in the high-resolution TEM image. Weak spots corresponding to the superlattice reflections of the bixbyite structure are present in the FFT diagram of Region A (dashed square), whereas only fundamental sports appear in the FFT diagram of Region B.

Figure 4. Structure of ion irradiated δ-$Sc_4Hf_3O_{12}$ after thermal annealing at 300 ^oC for 2 hr. (a,b) Electron diffraction patterns, (c) bright-field and (d) dark-field TEM images. The bixbyite phase originally existed in this region before annealing. The diffraction patterns correspond to those of (a) the δ- and (b) fluorite structures viewed along the $[\bar{1}11]$ and [112] directions, respectively. The dark-field image taken using the superlattice reflection of the δ-type structure; the bright and dark regions in (d) correspond to the δ and fluorite phases,

respectively. It is apparent that the δ-type phase is preferentially formed at the grain boundary.

Figure 5. *In-situ* TEM observations on thermally-induced structural changes. (a) Room temperature, (b) 180 ^{o}C for 5 min, (c) 200 ^{o}C for 5 min, (d) 200 ^{o}C for 10 min, and (e) 200 ^{o}C for 15 min. In (a), the ion-beam-induced bixbyite was present before annealing. No structural changes were observed in (b), while the superlattice spots of the δ-type phase appear in (c) and their intensity increases with thermal annealing (d). Finally, the diffuse spots due to the bixbyite phase disappear in (e).

Figure 6. Time evolution of selected-area electron diffraction patterns under 200-keV electron irradiation for (a) 0, (b) 1, (c) 3, and (d) 5 min. A bixbyite to δ phase transformation occurs with increasing the irradiation time. The diffraction pattern of (d) is a superposition of two (111) diffraction patterns with different variants.

Figure 7. (a) Selected-area electron diffraction pattern taken from the specimen irradiated with a 300 keV electron beam and (a') the dark-field image taken using two superlattice reflections of the δ-type structure. The dashed line in (a') denotes the irradiated area. (b,c) Nanobeam electron diffraction patterns taken by an electron beam with ~50 nm diameter. It is apparent that the selected-area diffraction pattern of (a) can be interpreted by the superposition of the diffraction patterns of (b) and (c). (b',c') Dark-field TEM images taken by a single superlattice spot in the diffraction pattern of (b,c). In the dark-field images in (b) and (c), different locations are brightened, indicating the presence of two variants of the δ-type structure.

Figure 8. Structural changes under 300-keV electron beams obtained by *in-situ* dark-field TEM observations. A superlattice spots of the δ-type structure was selected for the imaging. (a) Initial state (0 min), (b) 19 min, (c) 22 min, (d) 25 min, (e) 28 min, and (f) 32 min. Bright regions corresponding to the δ-type structure appear in (b), and their region and intensity increase with irradiation time, as seen in (c-f).

Figure 9. Selected-area electron diffraction patterns (a) before and (b) after 80-keV electron irradiation for 30

min. These diffraction patterns correspond to the (111) reciprocal plane of the bixbyite structure. In the diffraction pattern of the specimen irradiated for 30 minutes in (b), the spots due to the δ phase appears as indicated by arrows, but they are very weak and diffuse, suggesting that the structural change is significantly suppressed.

Supplemental data

Figure S1. Structural changes under 300-keV electrons obtained by *in-situ* dark-field TEM observations. The ~30-min video is fast-forwarded and edited down to 12 s. A superlattice spot of the *δ*-type were used for the imaging, and therefore the bright regions appearing after electron beam irradiation correspond to the *δ*-phase domains. Overall contrast is very weak at the initial stage of electron beam irradiation, because only the bixbyite and fluorite phases exists. The nucleation and growth of the *δ* phase was clearly observed with irradiation.

CRediT Author Statement

Masanari Iwasaki: Investigation, Data Curation, Visualization. **Maulik K. Patel**: Resources, Investigation, Writing- Review & Editing. **Gianguido Baldinozzi**: Investigation, Writing- Review & Editing. **Kurt E. Sickafus**: Conceptualization. **Manabu Ishimaru:** Supervision, Funding acquisition, Visualization, Writing- Original Draft.

Figure 1

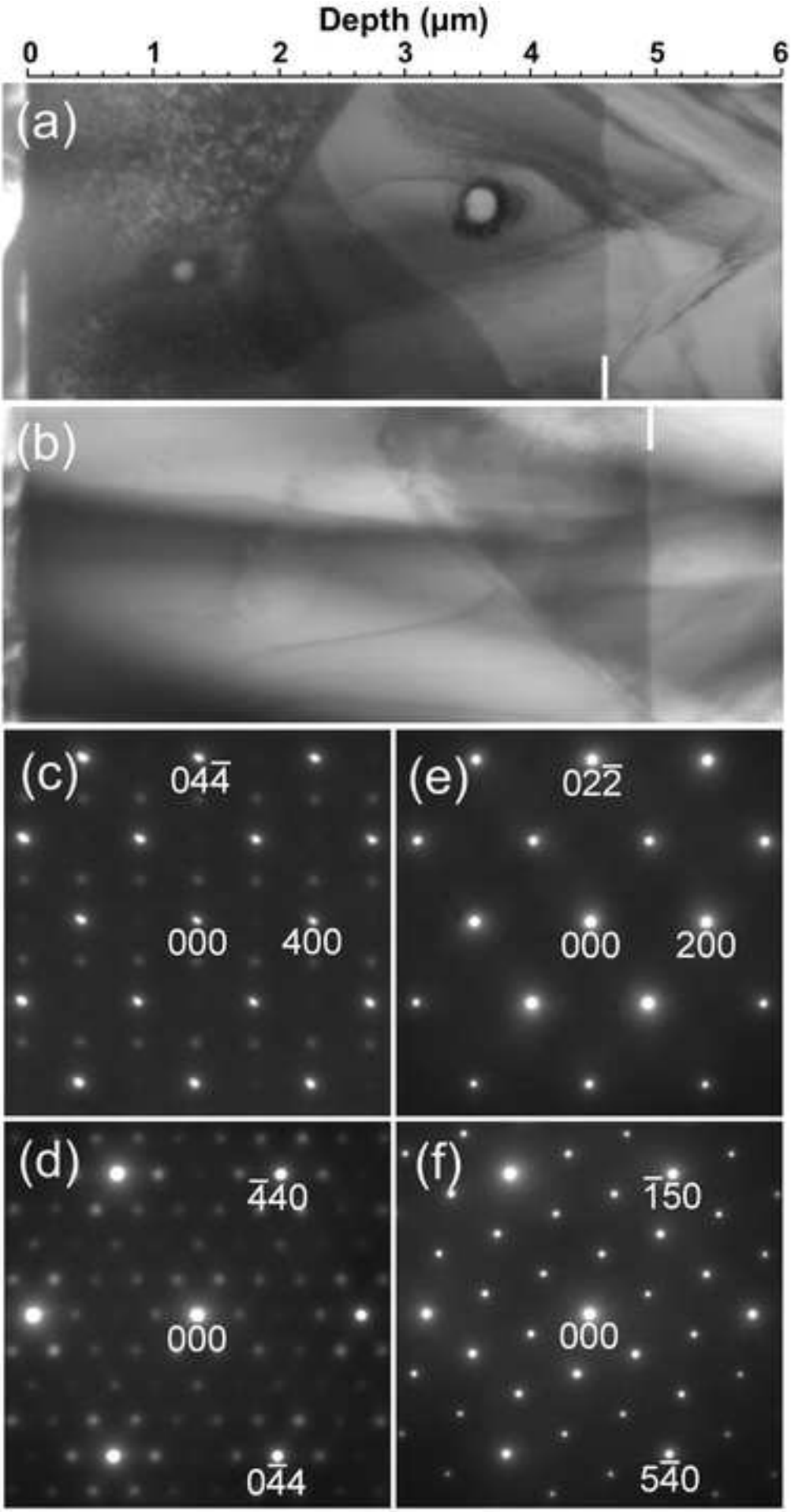

Figure 2

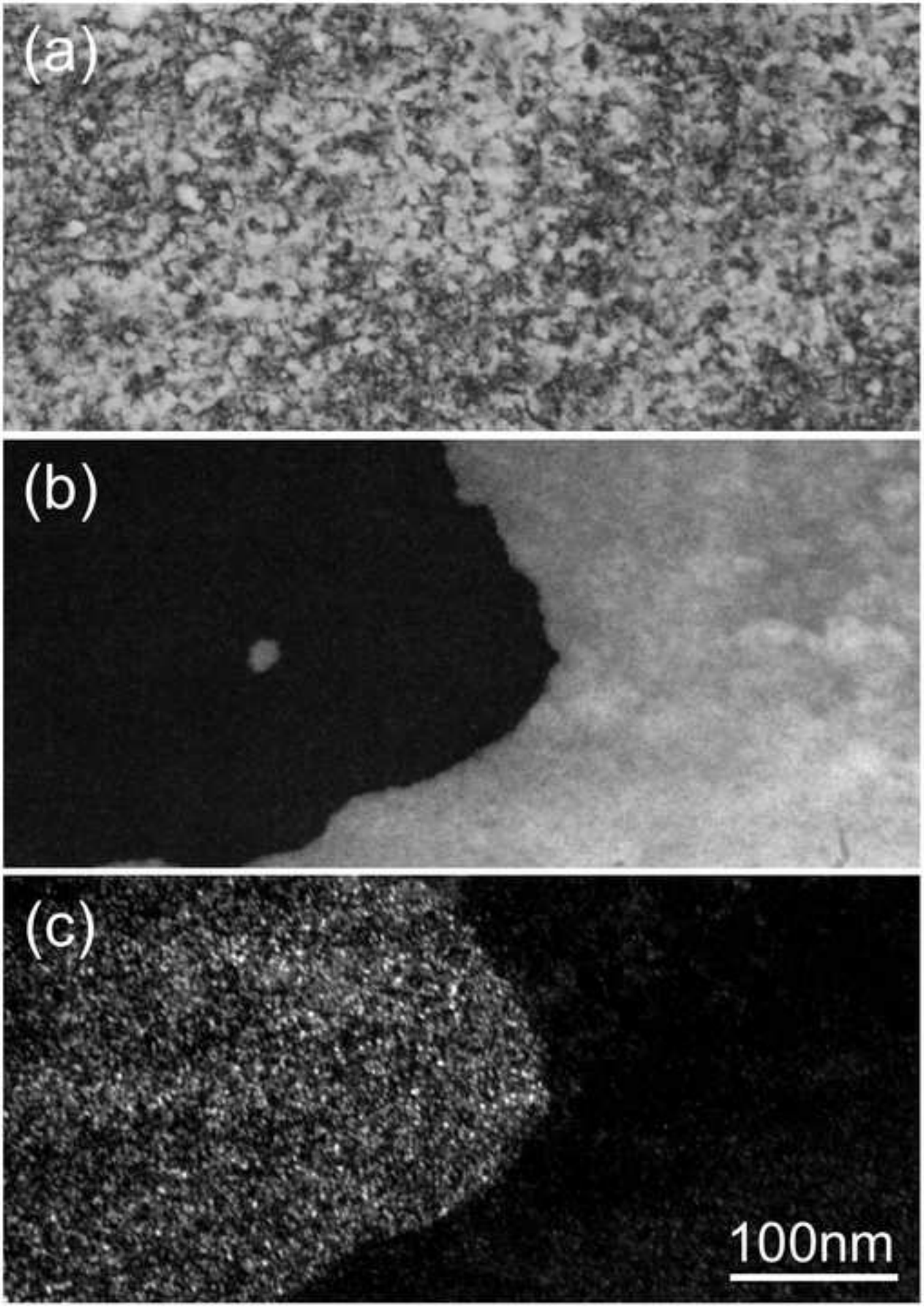

Figure 3

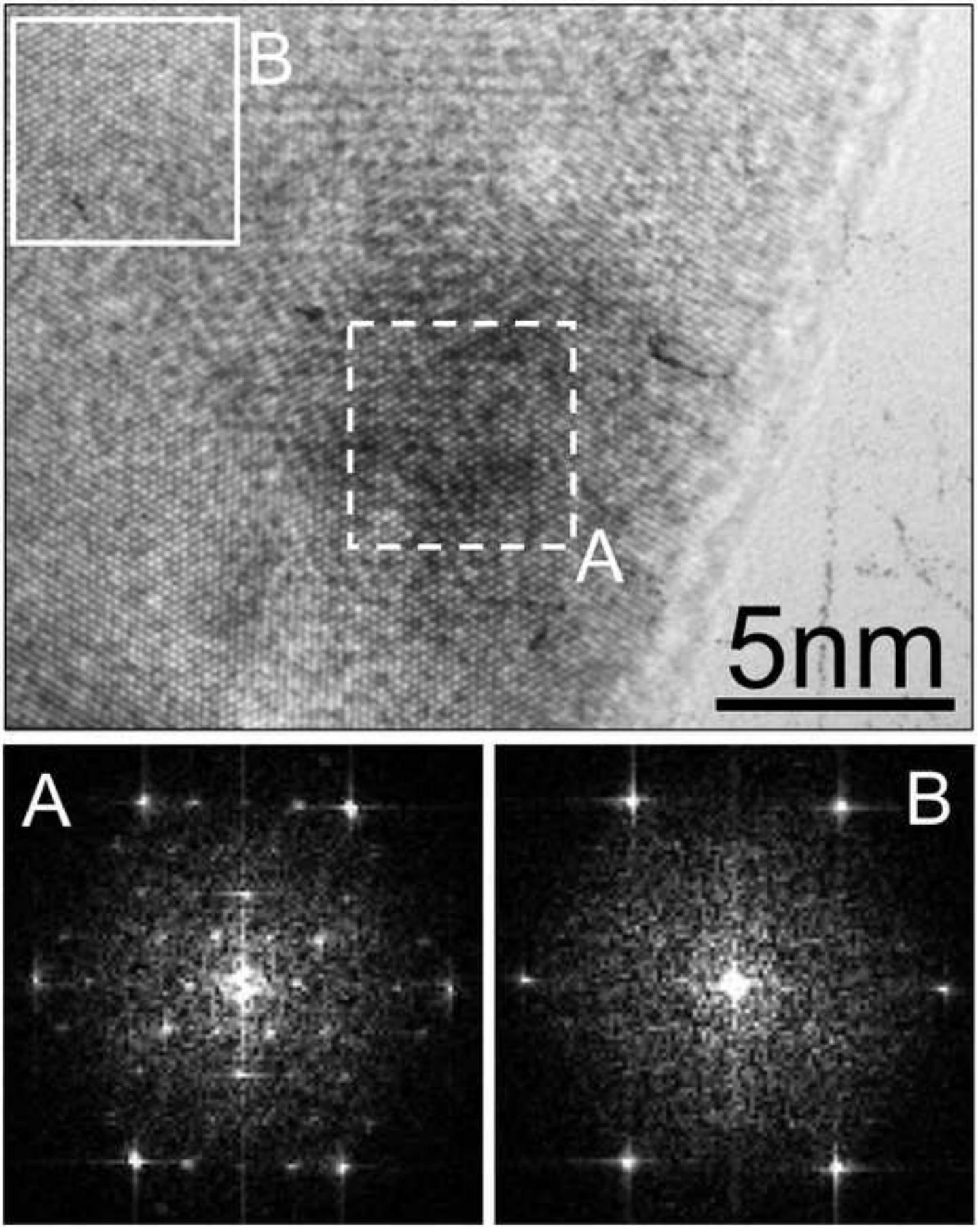

Figure 4

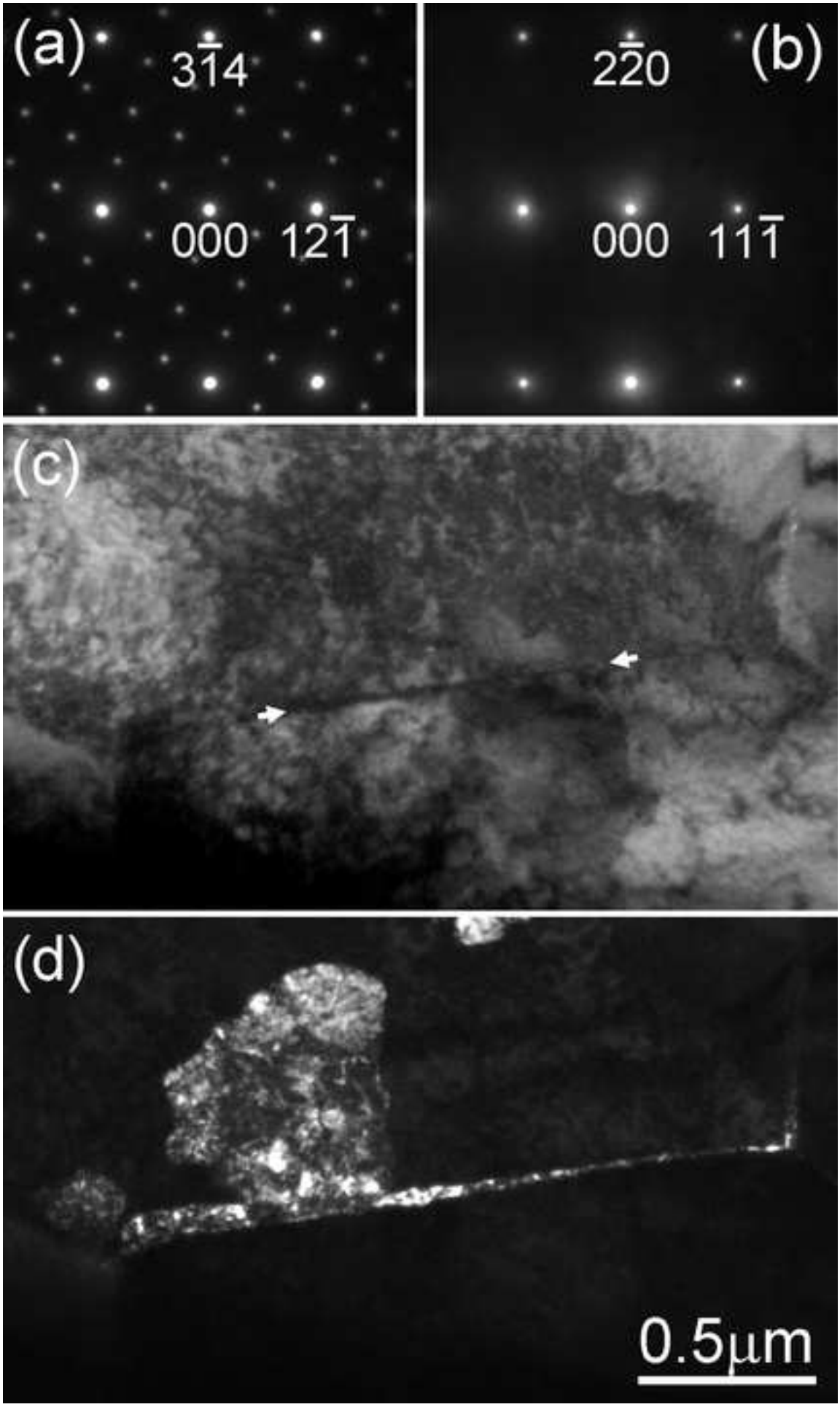

Figure 5

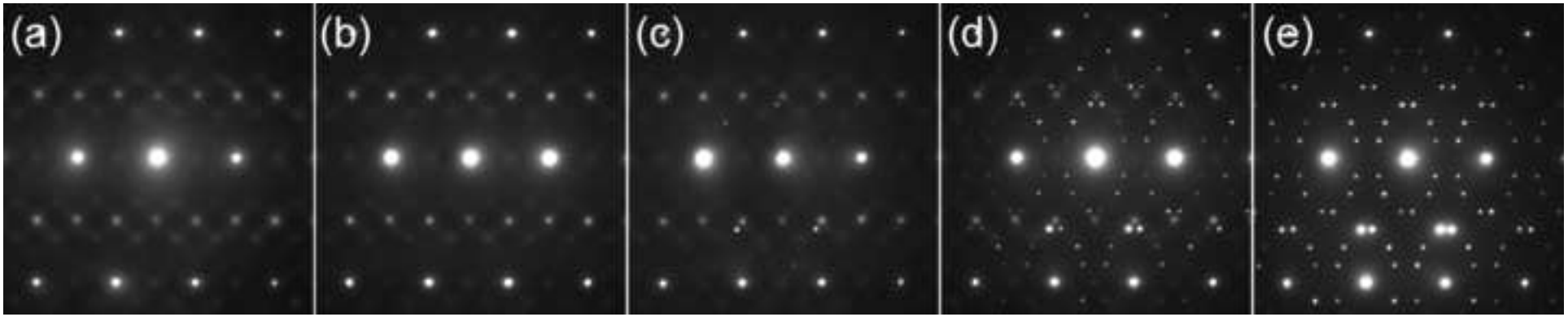

Figure 6

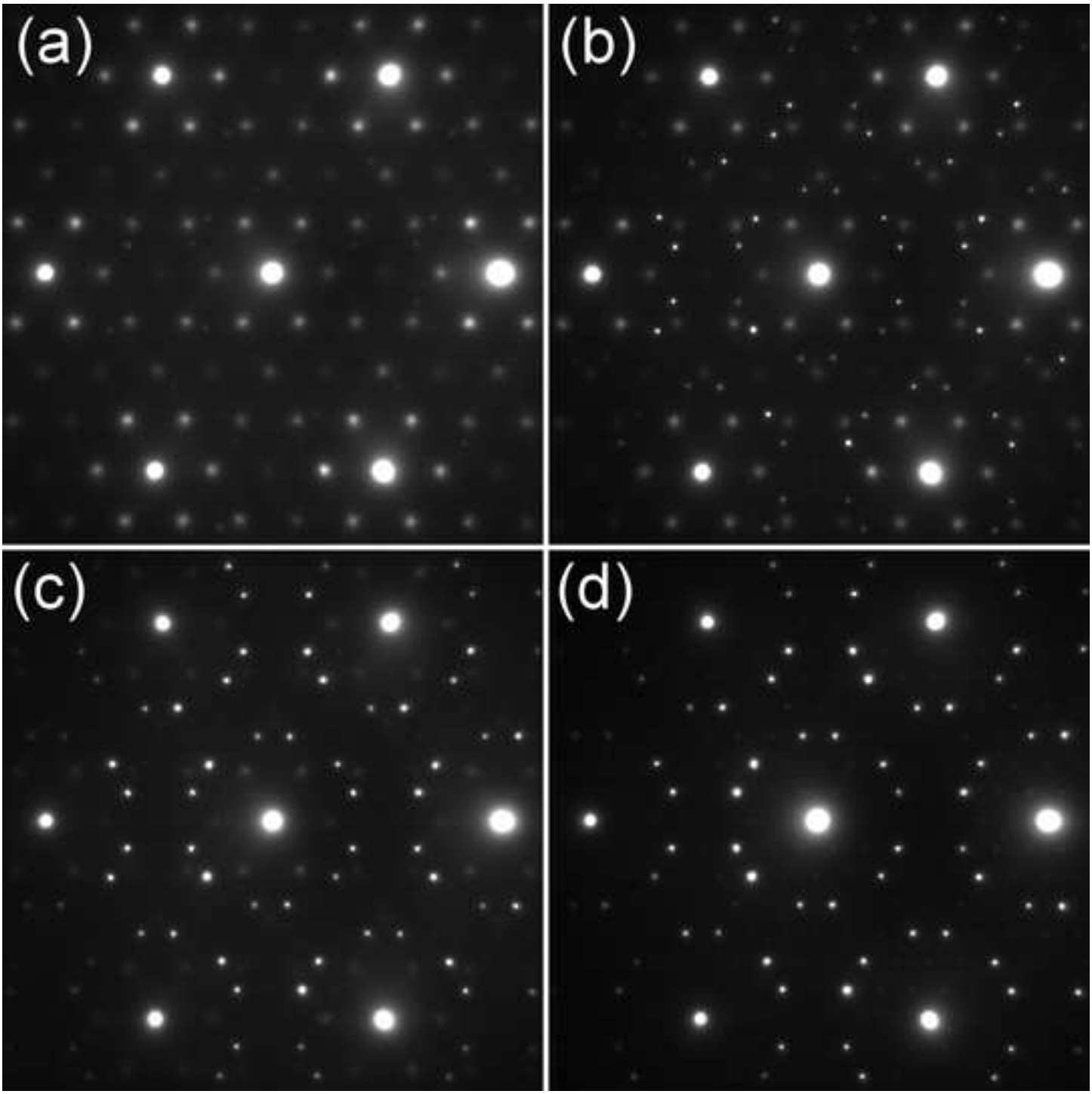

Figure 7

Click here to access/download;Figure;FIG7.jpg

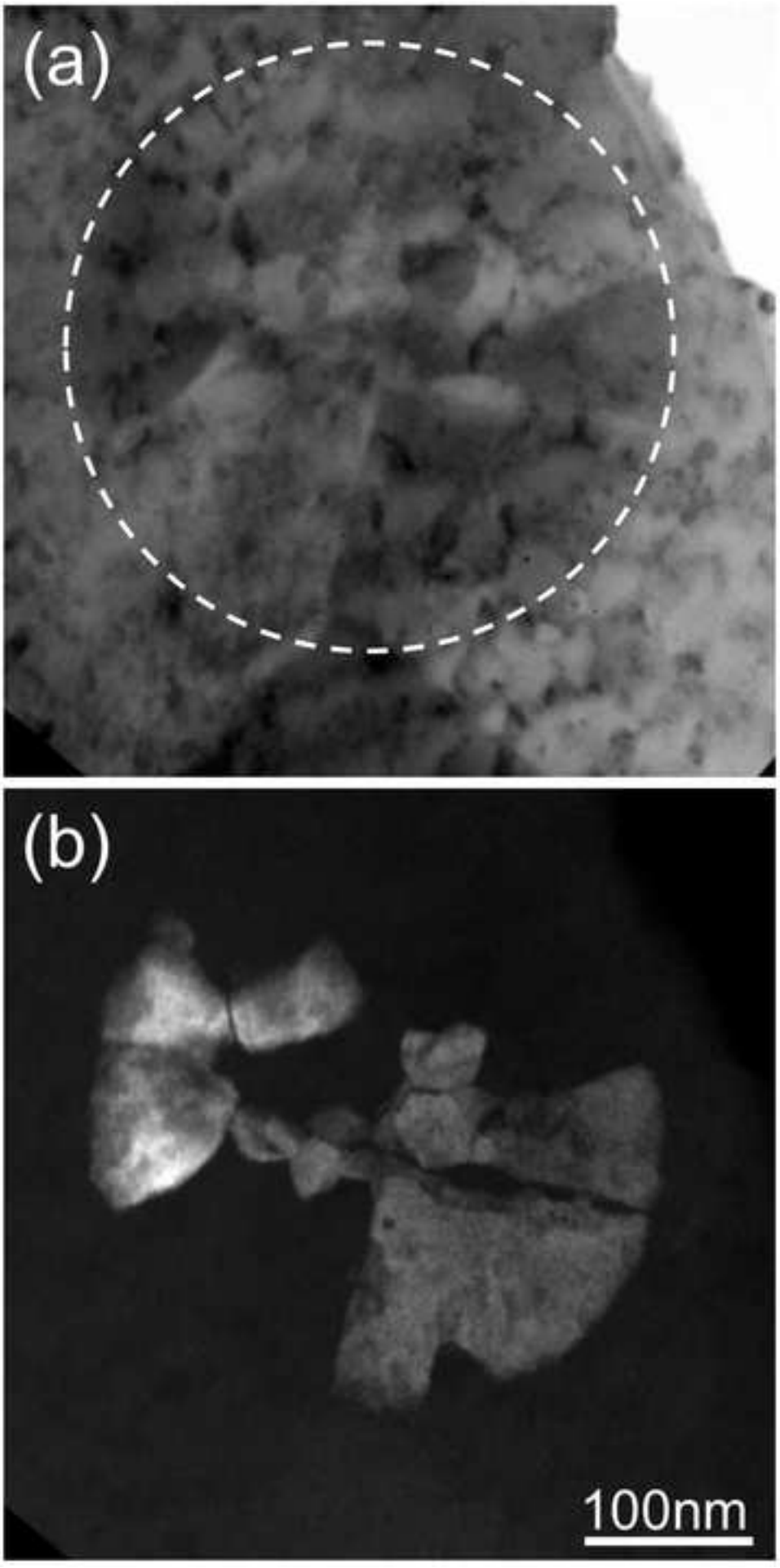

Figure 8

Click here to access/download;Figure;FIG8.jpg

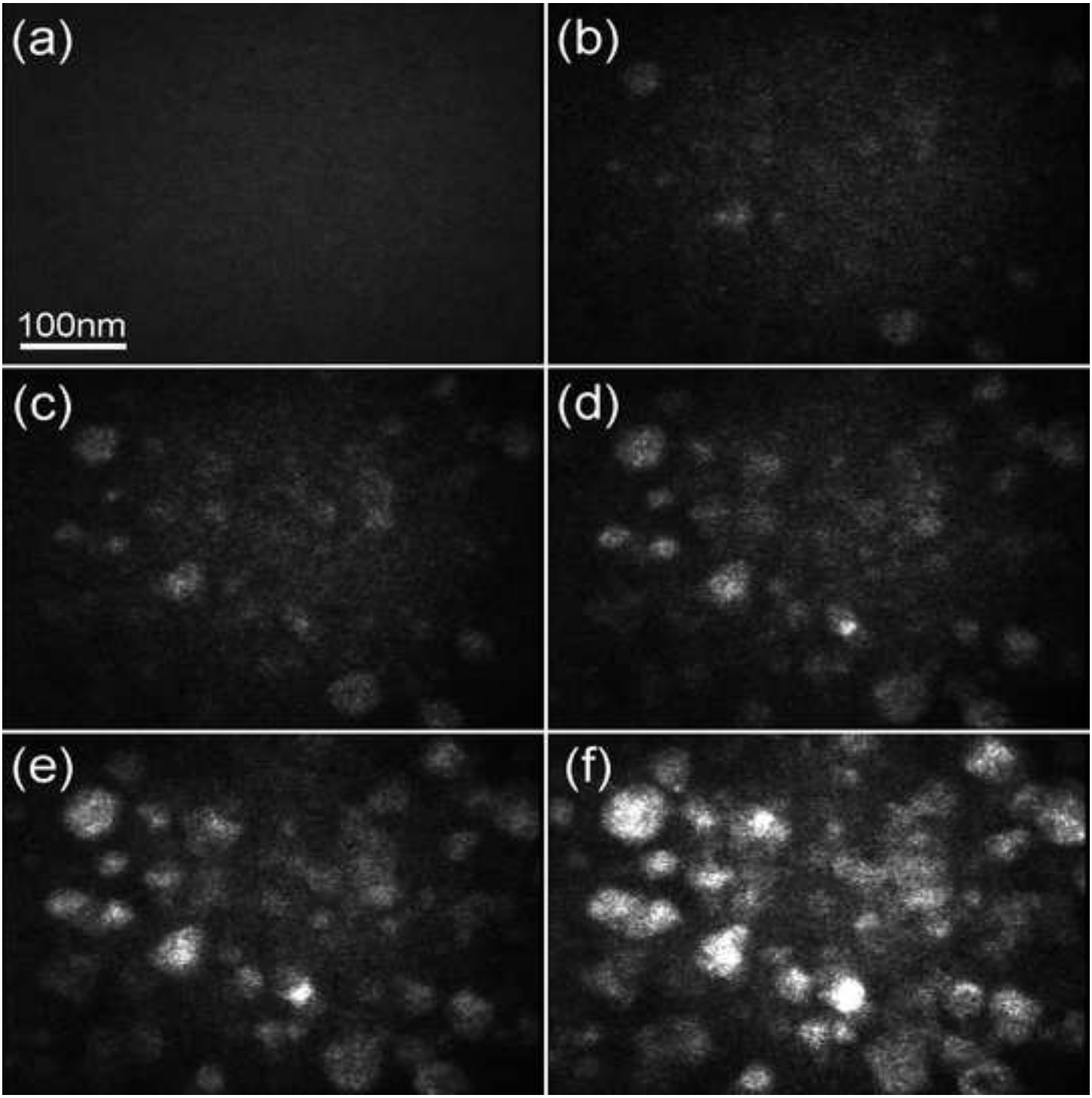

Figure 9

Click here to access/download;Figure;FIG9.jpg